

Cite this: DOI: 00.0000/xxxxxxxxxx

# Cell-substrate friction triggers complex fingering instabilities in spreading epithelial monolayers<sup>†</sup>

Carolina Trenado,<sup>a</sup> Luis L. Bonilla,<sup>a</sup> and Alejandro Martínez-Calvo<sup>b</sup>Received Date  
Accepted Date

DOI: 00.0000/xxxxxxxxxx

Collective cell migration plays a crucial role in many developmental processes that underlie morphogenesis, wound healing, or cancer progression. In such coordinated behaviours, cells are organised in coherent structures and actively migrate to serve different biological purposes. In some contexts, namely during epithelial wound healing, it is well known that a migrating free-edge monolayer develops finger-like instabilities, yet the onset is still under debate. Here, by means of theory and numerical simulations, we shed light on the main mechanisms driving the instability process, analysing the linear and nonlinear dynamics of a continuum compressible polar fluid. In particular, we assess the role of cell polarization, substrate friction, and contractile stresses. Linear theory shows that it is crucial to analyse the perturbation transient dynamics, since we unravel a plethora of crossovers between different exponential growth rates during the linear regime. Numerical simulations suggest that cell-substrate friction could be the mechanism responsible for the formation of complex finger-like structures at the edge, since it triggers secondary fingering instabilities and tip-splitting phenomena. Finally, we obtain a critical contractile stress characterising an active wetting-dewetting transition. In the dewetting scenario, the monolayer retracts and becomes stable without developing finger-like structures.

## 1 Introduction

Viscous fingering instabilities have been extensively studied since the seminal works of S. Hill<sup>1</sup>, R.L. Chuoke and coworkers<sup>2</sup>, P.G. Saffman and G.I. Taylor<sup>3</sup>, who observed and deduced that the interface between a moving fluid displacing another more viscous fluid in a Hele-Shaw cell<sup>4</sup> is unstable to small disturbances. The reader is referred to refs.<sup>5–9</sup> for detailed excellent reviews on hydrodynamic finger-like instabilities and pattern formation. Such interfacial instabilities have been also observed in several biological contexts during *in vivo* processes. In particular, fingering instabilities arise both, in prokaryotic systems, namely during bacterial growth<sup>10–15</sup>, and in eukaryotic group of cells, for instance during collective cell migration, which drives a myriad of crucial biological processes such as morphogenesis<sup>16–18</sup>, embryogenesis<sup>19,20</sup>, or tumour invasion<sup>21–25</sup>. Regarding collective cell migration, a huge interdisciplinary effort has been devoted to unravel the main physical mechanisms involved in these complex group behaviours, i.e. how cell-cell interactions can give rise to a cohesive coordinated motion<sup>26–30</sup>. Nonetheless, the key mecha-

nisms driving the emergence of fingering instabilities during collective cell migration is still under debate. As we detail below, the onset of instability might be a consequence of the complex coordinated behaviour of cells, involving the interplay between mechanical and chemical signals, and the interaction with their environment.

'Cell' was the word coined by the big-name British polymath Robert Hooke to name these closed units that form a complex organised structure<sup>31</sup>. In particular, the interaction between them and with the medium they inhabit, gives rise to highly correlated collective motion and mechanical stresses<sup>28</sup>. As a group, they usually become motile under chemical and mechanical stimuli, enabling development and regeneration processes. For instance, in embryogenesis and morphogenesis, cells grow significantly until they conform a global morphology, during wound healing, cells migrate to close a gap, and also in pathological processes such as tumor invasion, malignant cells migrate and grow invading healthy populations of cells.

In 1962, M. Abercrombie and E. Ambrose wrote 'It is a well-known principle that epithelium will not tolerate a free edge'<sup>21</sup>, meaning that, a free-edge two-dimensional epithelial sheet resting on a substratum, will migrate by an active pulling action of polarized cells located near the edge, until they reach a boundary or another epithelium. During this process, wound healing *in vivo* and *in vitro* experiments have revealed that the epithelium edge can form multi-cellular finger-like structures as it migrates

<sup>a</sup> Department of Mathematics, Gregorio Millán Institute, Fluid Dynamics, Nanoscience and Industrial Mathematics, Universidad Carlos III de Madrid, 28911 Leganés, Spain; E-mail: ctrenado@ing.uc3m.es

<sup>b</sup> Grupo de Mecánica de Fluidos, Gregorio Millán Institute, Fluid Dynamics, Nanoscience and Industrial Mathematics, Universidad Carlos III de Madrid, 28911 Leganés, Spain; E-mail: amcalvo@ing.uc3m.es

to close the wound. Hence, wound healing is a very convenient biological process to study collective cell migration and the formation of fingering patterns. Nonetheless, the physical mechanisms responsible for such instability remain controversial. Some authors, by means of experiments<sup>26,29,32–36</sup>, theory and numerical simulations of continuum<sup>35–37</sup> and agent-based models<sup>36,38,39</sup>, argue that the existence of polarized leader cells at the edge and the signaling with their followers, may drive the emergence of finger-like protrusions by using an active pulling action. In a recent work<sup>25</sup>, numerical simulations of the active-vertex model suggest that leader cells are not necessary to trigger the fingering instability if the dynamics of cell centers includes collective tissue forces, velocity alignment, and inertia, which are the key mechanisms driving the instability. In a few recent works, linear stability analyses of continuum active fluid models have been derived to explain the experimental observations, arguing that the emergence of fingering instabilities could be explained by means of a kinematic hydrodynamic-like interfacial instability<sup>36,40–42</sup>.

Concerning the latter approach, this class of theoretical models aim to describe the epithelial monolayer as an active fluid or visco-elastic continuum by means of macroscopic fields such as velocity, displacement, cell density, and cell polarization. Refs.<sup>41,43,44</sup> study the linear stability of a two-dimensional incompressible active fluid modelled via Toner-Tu-like equations, in strip<sup>41,43</sup> and circular<sup>44</sup> configurations. The former works show that a quiescent monolayer is unstable to small perturbations for some ranges of wavenumbers depending on inertial effects, whereas a monolayer moving with uniform velocity is stable to all wavenumbers. Regarding the circular configuration, ref.<sup>44</sup> shows that an initially migrating monolayer is unstable when cell growth is taken into account. More recently, the work of<sup>36</sup> shows that the uniform-velocity migrating monolayer is unstable when considering leader cells at the interface, in the absence of cell growth. In this work, leader cells are taken into account within the continuum framework by introducing a curvature-dependent force at the interface, similarly to the work of<sup>45</sup>, where the interface is modelled as an elastic membrane with bending resistance via the Helfrich-Canham potential<sup>46–51</sup>.

In a series of recent works<sup>24,30,42,52–55</sup>, the epithelial monolayer is modelled as a compressible viscous polar fluid, taking into account contact active forces between cells, cell-substrate friction, viscous, surface tension, and contractile forces. Ref.<sup>42</sup> shows that the flat-front solution becomes unstable by means of a kinematic mechanism: when a small perturbation is introduced at the edge, the gradient of velocity across the monolayer, which comes from the balance between contact-active and viscous forces, makes the crests to move faster than the valleys. However, these works do not explore the time-dependent stability of the migrating monolayer, something that we believe is crucial to assess the stability and the most amplified wavelengths, since the velocity profile is not uniform and the velocity at the edge is not generically constant. Additionally, the effect of these forces in the nonlinear regime remains almost unexplored, which is essential to unravel the main mechanisms driving the instability and to assess if this kind of active continuum modelling is able to qualitatively reproduce the experimental observations. Other works have explored

the long-time behaviour of spreading monolayers via numerical simulations of similar continuum models<sup>56,57</sup>. Ref.<sup>56</sup> takes into account time-dependent, inertial and corotational effects in cell polarization, as well as viscoelastic effects via the Maxwell model. Ref.<sup>57</sup> considers a neo-Hookean elastic material taking into account cell proliferation, stress-polarization coupling, as well as long-range chemo-mechanical interactions, i.e. a feedback loop between tissue deformation and inter-cellular chemical signaling. Both works obtain finger-like patterns at the edge, some of them qualitatively similar to the ones observed in the experiments. Nonetheless, these works do not systematically explore the role of the different forces involved during the migration, and which are the key mechanisms underlying these complex patterns in the nonlinear regime.

Hence, by using the same continuum framework as in refs.<sup>24,30,42,52–55</sup>, our work aims to distill the role of viscous, contact active, contractile forces and cell-substrate friction, which are ubiquitous during the migration of epithelial monolayers, on the linear and nonlinear regimes, by analysing the complete time-dependent linear stability, and via time-dependent numerical simulations to explore the long-time behaviour.

The paper is organised as follows. In Sec 2 we describe the active continuum model to analyse the collective dynamics of a two-dimensional cell sheet. In Sec 3, we briefly describe the procedure to obtain the base-flow and the corresponding linear stability analysis of such flow configuration. In Sec 4, we compare the results obtained from the linear stability analysis and the time-dependent two-dimensional numerical simulations of the complete equations of motion. Using both frameworks, we consider different distinguished limits to discuss the role of the governing physical parameters on the migration, stability, and spreading nonlinear regimes of the epithelial sheet. Conclusions are drawn in Sec 5, where we also discuss future theoretical avenues in understanding the collective behaviour of epithelial monolayers.

## 2 Theoretical modeling

To analyse the collective cell dynamics of a spreading epithelial monolayer we adopt the same theoretical continuum framework as in refs.<sup>24,30,42,52–55</sup>, mainly inspired by active-gel physics<sup>60</sup> and liquid crystal theory<sup>61</sup>. In particular, we consider an active polar fluid surrounded by a passive ambient, propagating in the direction perpendicular to its interface due to contact active forces (see the sketch in Fig. 1a). The flow is described in terms of the polarity field  $\mathbf{p}$ , which takes into account the alignment and direction of active units, and the velocity field  $\mathbf{u}$ . We assume that the flow is two-dimensional, thus  $\mathbf{u}$  and  $\mathbf{p}$  are depth-average fields. This assumption provides a good approximation if the slip length is significantly larger than the layer thickness<sup>62–64</sup>, which may be the case for thin epithelial monolayers. We further assume that the flow is compressible, and neglect inertial effects and internal pressure due to cell proliferation. The spontaneous spreading process is triggered by contact active forces proportional to  $\mathbf{p}$ , which we assume to be in balance with viscous forces. Within the stress balance, we also consider cell-substrate friction and contractile forces, disregarding flow alignment, and the elastic response of the tissue. For the sake of simplicity, the shear and

Physical Parameters	Definition	Range of values	
$\ell$	Monolayer initial width	100–400 $\mu\text{m}$	42,52
$\mu$	Shear viscosity	$10^4$ – $10^6$ Pa min	52,54
$h$	Tissue height	5 $\mu\text{m}$	54,58
$T$	Traction coefficient	0.1–0.5 kPa	52,54
$L_c$	Nematic length	20–100 $\mu\text{m}$	52,54
$\zeta$	Intercellular contractility	–20 kPa	54
$\xi$	Cell-substrate friction	$10^4$ – $10^6$ Pa min $\mu\text{m}^{-2}$	52
$\gamma$	Surface tension coefficient	1–10 mN $\text{m}^{-1}$	59
Dimensionless Parameters			
$\Lambda = \ell/L_c$	Initial-to-nematic length ratio	1 – 8	
$\beta = \xi \ell^2/\mu$	Friction-to-viscous forces ratio	0.04 – 3.2	
$\alpha = \zeta h/(\ell T)$	Contractile-to-active-contact forces ratio	-10 – -0.5	
$Ca = \gamma h/(\ell^2 T)$	Active Capillary number	$10^{-4}$ – 0.05	

**Table 1** Estimates and experimental measurements of the physical parameters and estimated values of the dimensionless numbers.

bulk viscosity coefficients are assumed to be equal. For cell polarization dynamics, we consider a diffusion-dominated polarization field, neglecting advection, corotation, and flow alignment effects, i.e. negligible back-coupling of the flow on the polarization field.

The above physical mechanisms aim to explain the complex behaviours arising in a migrating epithelial monolayer, namely the formation of finger-like structures at the edge during the spreading process.

To non-dimensionalise the equations of motion, we assume that viscous and contact active forces are in balance, which yields,  $\mu \partial_x u_y \sim T/h$ , where  $u_y$  is the velocity across the monolayer (see Fig. 1a),  $\mu$  denotes the shear viscosity coefficient,  $h$  is the height of the tissue measured from the substrate, and  $T$  is a traction coefficient accounting for contact active forces of polarized cells. Hence, the characteristic velocity reads,  $u_c \sim T \ell^2/(\mu h)$ , where  $\ell = \bar{L}(t=0)$  is the initial width of the monolayer. It proves to be convenient to introduce the following non-dimensionalization

$$\mathbf{x} = \frac{\bar{\mathbf{x}}}{\ell}, \quad \mathbf{u} = \bar{\mathbf{u}} \frac{\mu h}{\ell^2 T}, \quad t = \bar{t} \frac{\ell T}{\mu h}, \quad L = \frac{\bar{L}}{\ell} \quad (1)$$

where bars denote dimensional variables,  $\mathbf{x}$ ,  $t$ , and  $L$ , are the position vector, time, and the monolayer half-width, respectively.

Considering the above assumptions, the equation for the polarization field  $\mathbf{p}(\mathbf{x}, t)$  is flow-independent and reads,

$$\nabla^2 \mathbf{p} = \Lambda^2 \mathbf{p}, \quad (2)$$

where  $\Lambda = \ell/L_c$  is the dimensionless parameter comparing the initial width of the monolayer  $\ell$ , and the characteristic decay length of the polarity field, denoted by  $L_c$ .

The dynamics of the epithelial monolayer is described through the following inertialess stress balance,

$$\nabla \cdot \boldsymbol{\sigma} + \mathbf{f} = \mathbf{0}, \quad (3)$$

where  $\boldsymbol{\sigma} = \nabla \mathbf{u} + (\nabla \mathbf{u})^T - \alpha \mathbf{p} \mathbf{p}$  is the stress tensor accounting for viscous and contractile forces,  $\alpha < 0$  being the dimensionless

signature of the active stress. The external body force reads:  $\mathbf{f} = -\beta \mathbf{u} + \mathbf{p}$ , which takes into account cell-substrate friction and contact active forces, respectively. In particular, the coarse-grained friction is assumed to be spatially uniform for simplicity. The dimensionless parameters are:  $\alpha = \zeta h/(\ell T)$  and  $\beta = \xi \ell^2/\mu$ , which compare inter-cellular contractile forces with contact active forces, and friction forces with viscous forces, respectively, where  $\zeta$ , and  $\xi$  are the dimensional contractility and cell-substrate friction coefficients. Furthermore, the dimensionless number  $\beta$  is also defined as the squared ratio between the initial length of the monolayer,  $\ell$ , and the screening length,  $\sqrt{\mu/\xi}$ , which characterises the penetration of the viscous stress inside the monolayer.

We impose the following kinematic boundary condition:

$$(\partial_t \mathbf{x}_s - \mathbf{u}) \cdot \mathbf{n} = 0 \quad \text{at} \quad y = L(x, t), \quad (4)$$

where  $\mathbf{x}_s$  is the parameterisation of the interface, and  $\mathbf{n}$  its unit normal vector. Additionally, we also impose that the polarization field is normal to the interface, and the surface stress balance:

$$\mathbf{p} = \mathbf{n}, \quad \text{and} \quad \boldsymbol{\sigma} \cdot \mathbf{n} + Ca(\nabla_s \cdot \mathbf{n})\mathbf{n} = \mathbf{0} \quad \text{at} \quad y = L(x, t), \quad (5)$$

where  $\nabla_s \cdot \mathbf{n} = -\partial_x^2 L[1 + (\partial_x L)^2]^{-3/2}$  is twice the mean curvature of the interface,  $\nabla_s = (\mathbf{I} - \mathbf{nn}) \cdot \nabla$  is the surface gradient operator, and  $Ca = \gamma h/(\ell^2 T)$  is an active Capillary number based on contact active forces. For the sake of simplicity, we have neglected the effect of interfacial tension, although as shown in Table 1, it may become relevant in some situations. Equivalently to the classical hydrodynamic instability, surface tension has a stabilising effect, as shown in ref.<sup>42</sup>, by generating an interfacial stress that tries to flatten the initial perturbation at the edge. Hence, the governing dimensionless parameters are  $\Lambda$ ,  $\beta$ , and  $\alpha$ , whose typical values are given in Table 1, using different estimates and experimental measurements of the physical parameters available in the literature.

We numerically integrate eqns (2)-(5) imposing that the monolayer is not polarized at the centre line, together with symmetry

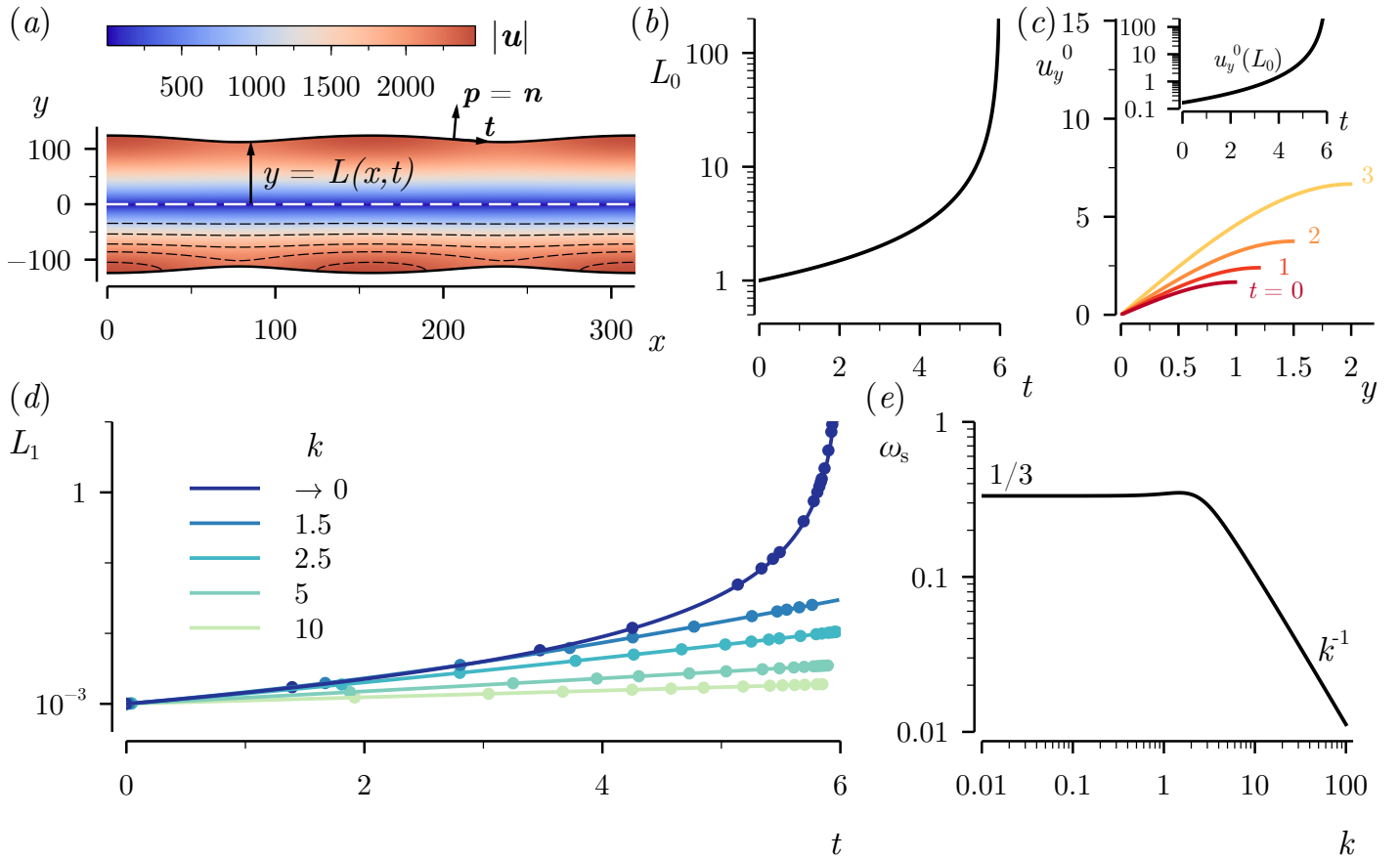


**Fig. 1** (a) Scheme of the monolayer obtained from a time-dependent numerical simulation of the complete equations of motion (2)-(7) with  $\Lambda = \beta = \alpha = 0$  and  $k = 0.04$  at  $t = 5.95$ . (b) Position of the base-flow interface  $L_0$  as a function of time  $t$ . (c) Base-flow velocity  $u_y^0$  as a function of  $y$  for different times indicated in the labels. The inset shows the velocity at the edge of the monolayer  $y = L_0$  as a function of time  $t$ . (d) Perturbation amplitude  $L_1$  as a function of time  $t$ , for different values of the wavenumber  $k$  indicated in the legend. (e) Short-time exponential growth rate  $\omega_s$  as a function of  $k$ .<sup>42</sup>

boundary conditions:

$$p_y = \partial_y p_x = u_y = \partial_y u_x = 0 \quad \text{at } y = 0, \quad (6)$$

and symmetric boundary conditions at the planes  $x = 0$  and  $x = \pi/k$ . To trigger the fingering instability, the interface of the spreading monolayer is slightly perturbed by a harmonic disturbance at  $t = 0$ ,

$$L(x, 0) = 1 - L_{1,0} \cos(kx), \quad (7)$$

for  $0 \leq x \leq \pi/k$ , where  $k$  is the wavenumber, and  $L_{1,0} \ll 1$  is the relative amplitude of the perturbation. The initial conditions for  $\mathbf{p}$  and  $\mathbf{u}$  are not imposed, since we employ a standard Newton-Raphson root-finding algorithm to obtain them with the above boundary conditions. For the time discretisation, we use a variable-step BDF method with 2/5 variable order, and the Arbitrary Lagrangian-Eulerian method within a finite-element framework to numerically solve the time-dependent free-boundary problem. In particular, the numerical technique is the same as the one employed in refs.<sup>65,66</sup>, where the reader can find further technical details.

### 3 Linear Stability Analysis

To analyse the migration and the stability of the epithelial monolayer, we perform a linear stability analysis considering the configuration shown in Fig. 1(a), which is commonly used in wound healing assays. To this end, we linearise the equations of motion around a certain base state and analyse the growth of small perturbations. In particular, we consider the unidirectional flat-front solution as base flow<sup>42</sup>, which reads:  $\mathbf{p}_0 = p_y^0(y)\mathbf{e}_y$  for the polarization field, and  $\mathbf{u}_0 = u_y^0(y)\mathbf{e}_y$ , for the velocity field. The detailed expressions of the base flow depending on the dimensionless parameters are given below. Once obtained  $\mathbf{p}_0$  and  $\mathbf{u}_0$ , the position of the base-flow interface,  $L_0(t)$ , is determined according to the kinematic condition (4), which simplifies to:

$$\frac{dL_0(t)}{dt} = u_y^0(y = L_0(t)). \quad (8)$$

To address the stability of the flat-front spreading monolayer, all the variables are perturbed around such base flow by small-amplitude disturbances. It is important to emphasise that the base state varies with time, thus the coefficients of the linearised equations of motion are also functions of time, which precludes the assumption of a simple exponential growth of disturbances.

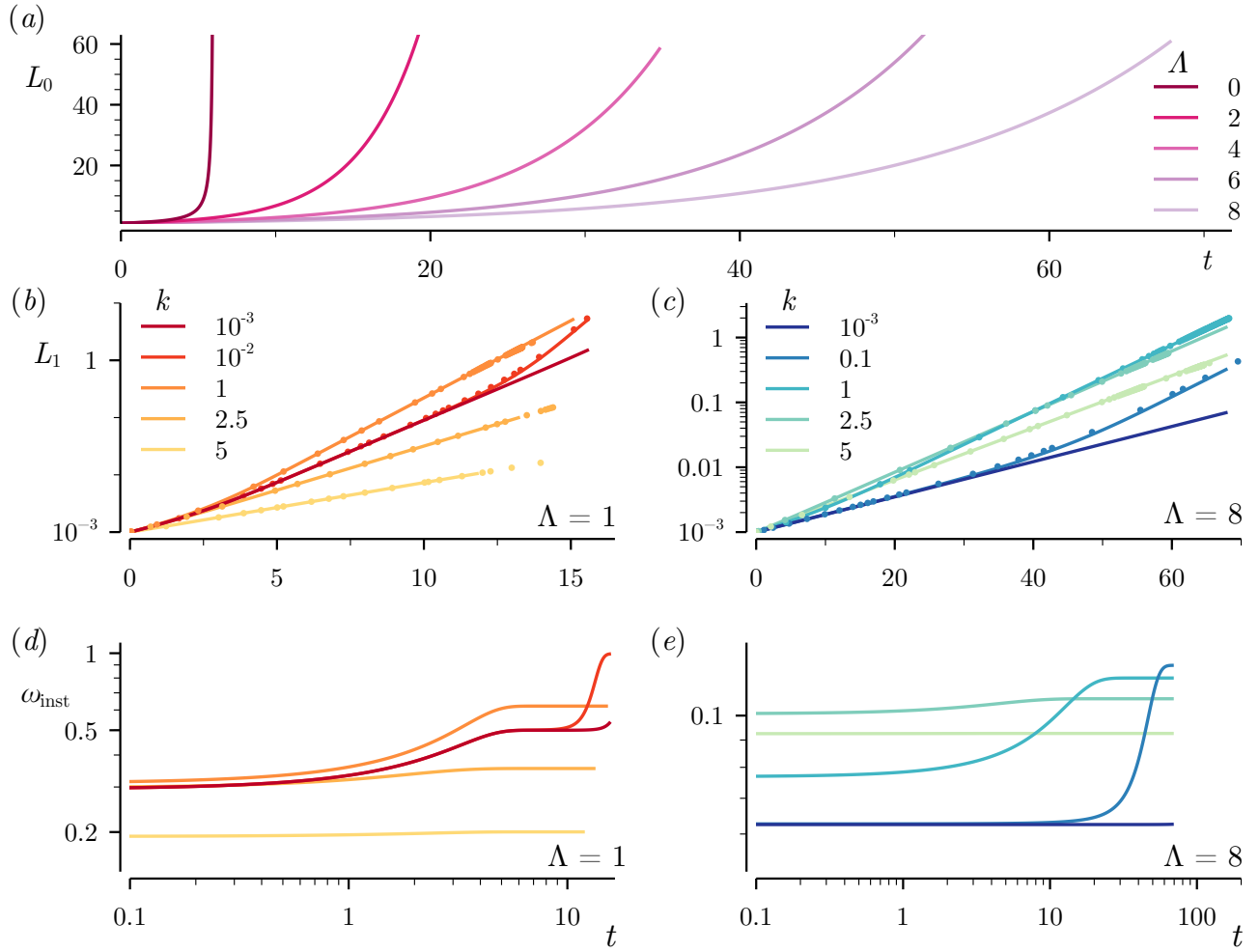


**Fig. 2** (a) Base-flow interface position  $L_0$  corresponding with the flat-front solution as a function of time  $t$ , for different values of  $\Lambda$  indicated in the legend. (b,c) Perturbation amplitude  $L_1$  as a function of time  $t$  for (a)  $\Lambda = 1$  and (b)  $\Lambda = 8$ , and different values of the wavenumber  $k$  indicated in the legends. (c,d) Instantaneous exponent  $\omega_{\text{inst}} = d \ln(L_1) / dt$  as a function of time  $t$  for the same values of  $\Lambda$  and  $k$  as in panels (a,b).

Therefore, the time-dependent perturbations are decomposed as Fourier wave-like modes defined by the wavenumber  $k$ :

$$(\mathbf{p}, \mathbf{u}, L) = (\mathbf{p}_0, \mathbf{u}_0, L_0) + (\mathbf{p}_1, \mathbf{u}_1, L_1) \exp(ikx), \quad (9)$$

where  $|\mathbf{p}_1|, |\mathbf{u}_1|, |L_1| \ll 1$ . This means that an algebraic dispersion relation,  $D(k, \omega) = 0$ , between an exponential growth rate of perturbations  $\omega$  and the wavenumber  $k$ , cannot be derived.

Introducing eqn (9) into the system of eqns (2)–(3), allows us to solve  $\mathbf{p}_1$  and  $\mathbf{u}_1$ , with the appropriate linearised boundary conditions (5) and (6). Finally, the evolution of the interface perturbation  $L_1$  is obtained from the linearised kinematic condition (4):

$$\frac{dL_1}{dt} = \partial_y u_y^0 L_1 + u_y^1 = \omega(k, t) L_1 \quad \text{at } y = L_0(t), \quad (10)$$

where we have taken advantage that  $u_y^1$  is proportional to  $L_1$ , to define  $\omega(k, t)$  as the time-dependent growth rate. This allows us to solve eqn (10), which yields<sup>42</sup>

$$L_1(t) = L_{1,0} \exp\left(\int_0^t \omega(k, t) dt\right). \quad (11)$$

Hence, to study the linear stability of the spreading front, we shall analyse the transient dynamics of the perturbations.

## 4 Results and discussion

In this section, we analyse the linear and nonlinear dynamics of the migrating epithelial monolayer, considering different distinguished limits to distill the role of the forces involved in the spreading process. To this end, we employ the linear stability analysis described above and time-dependent numerical simulations of the complete set of eqns (2)–(7).

### 4.1 Parameter-free solution: balance of viscous and contact active forces

We first consider the distinguished limit where  $\Lambda = \beta = \alpha = 0$ . In this limiting case, the base-flow polarity and velocity fields simplify to

$$\mathbf{p}_0 = \frac{y}{L_0} \mathbf{e}_y, \quad \text{and} \quad \mathbf{u}_0 = \frac{yL_0}{4} \left(1 - \frac{y^2}{3L_0^2}\right) \mathbf{e}_y. \quad (12)$$

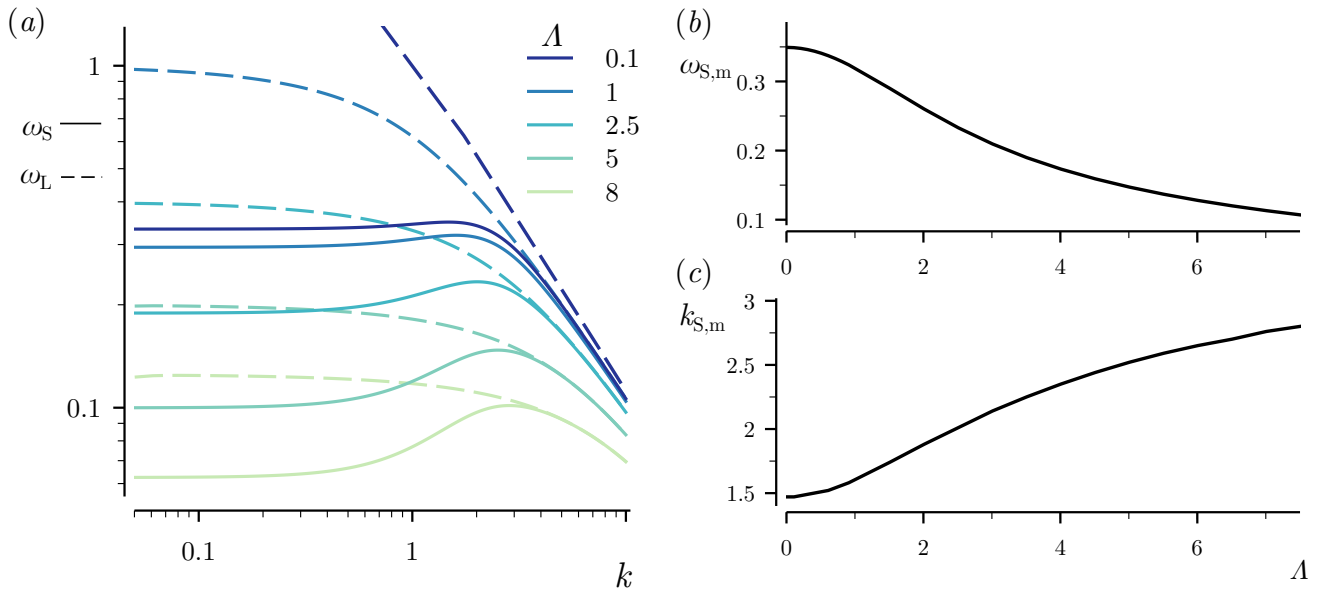


**Fig. 3** (a) Short-time  $\omega_s$  and large-time exponential growth rate  $\omega_L$  as functions of the wavenumber  $k$  in solid and dashed lines, respectively. (b) Maximum short-time growth rate  $\omega_{S,m}$  and (c) the corresponding most amplified wavenumber  $k_{S,m}$  as functions of  $\Lambda$ .

Hence, the evolution of  $L_0(t)$  can be straightforwardly obtained via the kinematic condition (8),  $dL_0/dt = L_0^2/6$ , which yields:  $L_0(t) = (1 - t/6)^{-1}$ . The temporal evolution of  $L_0$  and  $\mathbf{u}_0$  is shown in Figs. 1(b,c). This simplified base-flow solution grows linearly with time for  $t \ll 1$ , but experiences a singularity at  $t = 6$  where  $L_0$  and the edge velocity  $u_y^0(L_0)$  diverge. This non-physical behaviour is a consequence of the crude simplifications within the modelling.

Fig. 1(d) shows the perturbation amplitude  $L_1$  as a function of time  $t$ , for different values of the wavenumber  $k$  indicated in the legend, obtained from the linear stability analysis (eqn (10)) (solid lines), and from the two-dimensional numerical simulations of the complete equations of motion (filled circles). Initially, the growth of  $L_1$  is exponential for all values of  $k$ . In particular, for small values of  $k$ , this initial exponential growth is observed only at very short times, whereas when the value of  $k$  increases, the exponential growth lasts longer and the instantaneous growth rate  $\omega_{\text{inst}} = d(\ln(L_1))/dt = dL_1/dt/L_1$  varies very slightly with respect to the initial plateau. We have denoted this initial exponential growth rate as  $\omega_s(k)$ , which is shown in Fig. 1(e) as a function of  $k$ , evidencing that in this limit all the perturbation wavelengths are unstable, as already shown in ref. <sup>42</sup>. Here we also show that  $\omega_s$  exhibits a maximum value at finite  $k$ , namely  $k \simeq 1.48$ , which was also reported in ref. <sup>42</sup>, where the authors analyse the growth rate  $\omega(k, t)$  for a frozen value of  $L_0$ . Beyond this value,  $\omega_s$  decreases as  $k^{-1}$  and for  $k = 0$ ,  $\omega = 1/3$ .

However, to assess the dynamical stability of the spreading front, it is important not only to analyse the short-time behaviour, but the complete time evolution of the perturbation amplitude  $L_1$ . Indeed, although the amplitude grows initially faster at relatively large values of  $k$ ,  $L_1$  eventually grows faster at small values of  $k$ , as shown by Fig. 1(d), thereby evidencing the significance of analysing the whole time evolution. In particular, for  $k \lesssim 0.05$ ,

$L_1(t)$  becomes independent of  $k$ , except very close to  $t = 6$ , where  $L_1$  still grows faster as the value of  $k$  decreases. It is also important to emphasise that, even if  $L_1 \sim O(1)$ , the linear stability analysis still accurately describes the evolution of the migrating monolayer, which means that the perturbation remains spatially harmonic during most of the spreading process.

## 4.2 The role of edge polarization

Here we discuss the effect of edge polarization and weak bulk polarization, by considering finite values of the dimensionless parameter  $\Lambda$ , while still keeping  $\alpha = \beta = 0$ . In this limiting case, the polarization and velocity fields of the flat-front solution read, respectively,

$$\mathbf{p}_0 = \frac{\sinh(\Lambda y)}{\sinh(\Lambda L_0)} \mathbf{e}_y, \quad (13a)$$

$$\mathbf{u}_0 = \frac{1}{2\Lambda \sinh(\Lambda L_0)} \left( \cosh(\Lambda L_0) y - \frac{\sinh(\Lambda y)}{\Lambda} \right) \mathbf{e}_y. \quad (13b)$$

Although it becomes more cumbersome, the linear stability analysis is performed equivalently as in the previous section. In the present case, motivated by experimental measurements <sup>52,54</sup>, we have considered two different values of  $\Lambda$ , namely  $\Lambda = 1$  and  $\Lambda = 8$ , to analyse the effect of the cell polarization through the monolayer. When  $\Lambda = 1$ , the cell polarization decays with a characteristic length comparable to  $\ell$ , whereas when  $\Lambda = 8$ , only cells located close to the edge of the monolayer experience such polarization, and the bulk remains weakly polarized. Fig. 2(a) shows the time evolution of  $L_0$  for different values of  $\Lambda$ , evidencing that the monolayer spreading velocity is larger as the value of  $\Lambda$  decreases, since the polarization field  $\mathbf{p}$  does not rapidly decay close to the interface. In particular,  $L_0$  grows exponentially with time, with an  $e$ -fold time that increases with  $\Lambda$ , namely

$L_0 \sim \exp[t/(2\Lambda)]^{42}$ .

Additionally, Figs. 2(b,c) show the perturbation amplitude  $L_1$  for  $\Lambda = 1$  and  $\Lambda = 8$ , respectively, and different values of the wavenumber  $k$  indicated in the legends. In particular, solid lines are obtained from linear theory and filled circles corresponds with the results obtained from the time-dependent numerical simulations. Here we also observe that, for finite values of  $\Lambda$ , the perturbation remains spatially harmonic even when  $L_1$  is of order unity, yielding and excellent agreement between linear theory and numerical simulations. Besides, equivalently to the dynamics of the base-flow solution, the perturbation amplitude  $L_1$  also grows faster as the value of  $\Lambda$  decreases. To analyse the transient dynamics of  $L_1$ , Figs. 2(d,e) show the instantaneous growth rate  $\omega_{\text{inst}}$  as a function of time  $t$ , revealing that for finite values of  $\Lambda$ ,  $L_1$  experiences several crossovers between different exponential regimes depending on the value of  $k$ , in contrast to the limiting case of  $\Lambda = 0$  due to the finite-time singularity. Thereby, as in Section 4.1, we define a short-time and also a long-time exponential growth rate, denoted by  $\omega_S$  and  $\omega_L$ , respectively, which are shown in Fig. 3(a) as functions of  $k$ , for different values of  $\Lambda$  indicated in the legend. In the case of  $\omega_L$ , it is only well defined when  $\omega_{\text{inst}}$  reaches a plateau for  $t \gg 1$ , and it is obtained numerically by imposing the criterion  $d\omega_{\text{inst}}/dt < 10^{-2}$ .

Both, short-time (solid lines) and long-time (dashed lines) growth rates decrease monotonically as the value of  $\Lambda$  increases for every value of  $k$ . The most-amplified short-time growth rate occurs at finite  $k$  for every value of  $\Lambda$ , as already pointed out in the limiting case  $\Lambda = 0$ , discussed in Section 4.1<sup>42</sup>. Figs. 3(b,c) show the maximum short-time growth rate  $\omega_{S,m}$  and the corresponding most-amplified wavenumber  $k_{S,m}$  as functions of  $\Lambda$ . While the maximum short-time growth rate decreases with  $\Lambda$ , the most-amplified wavenumber increases monotonically with  $\Lambda$ . However, at long time, the most-amplified growth rate occurs at  $k \ll 1$ , with a maximum value that is larger than the maximum short-time growth rate for all values of  $\Lambda$ . At large values of  $k$ , namely  $k \gtrsim 5 - 10$ , short-time and long-time growth rates coincide, since the growth of  $L_1$  remains nearly exponential during the whole time evolution.

### 4.3 The role of substrate friction

In this section, we analyse the effect of cell-substrate friction in the limit where contractile stresses are negligible,  $\alpha = 0$ . In this particular case, the expression for the base-flow polarity field is identical to that of Section 4.2, and the flat-front velocity field reads:

$$\mathbf{u}_0 = \left[ \frac{\Lambda \cosh(\Lambda L_0) \sinh(\sqrt{\beta/2}y)}{\sqrt{\beta/2} \cosh(\sqrt{\beta/2}L_0) [(2\Lambda^2 - \beta) \sinh(\Lambda L_0)]} + \frac{\sinh(\Lambda y)}{\sinh(\Lambda L_0) (2\Lambda^2 - \beta)} \right] \mathbf{e}_y, \quad (14)$$

which is a positive function for  $y > 0$  and every value of the dimensionless parameters, and whose maximum value is located at edge of the monolayer as in the previous limiting cases.

The temporal evolution of  $L_0$  is shown in Figs. 4(a,b) for differ-

ent values of  $\beta$  indicated in the legend, (a)  $\Lambda = 1$ , and (b)  $\Lambda = 8$ . After a short transient, we observe that  $L_0$  grows linearly with time, in agreement with the experimental observations in ref.<sup>52</sup>, with a constant velocity  $V = 1/(\beta + \sqrt{2\beta}\Lambda)$ . As expected,  $L_0$  is slowed down by the action of cell-substrate friction.

Here we carry out the linear stability analysis in the same manner as in the previous cases. Figs. 4(c,d) display the time-dependent evolution of the perturbation amplitude  $L_1$  for different values of the wavenumber  $k$  indicated in the legend, (c)  $\Lambda = 1$ , (d)  $\Lambda = 8$ , and  $\beta = 0.1$ , extracted from linear theory (solid lines), and from numerical simulations (filled circles). Substrate friction has a stabilising effect on  $L_1$ , by comparing these results with those shown in Figs. 3(b,c) for  $\beta = 0$ . Additionally, at short time, the most amplified wavenumber is shifted towards larger values, as already pointed out in ref.<sup>42</sup>. More interestingly, for small values of  $k$ , the perturbation amplitude almost reaches a plateau within the linear regime, namely for  $k = 0.1$  in Figs. 4(c,d). However, as time evolves, the linear stability analysis cannot predict the growth of  $L_1$ , even though it is far from being of order unity. After the plateau,  $L_1$  increases with a larger slope than its short-time growth rate.

Figs. 4(e,f) display two snapshots of the spreading monolayer for the same values of  $\Lambda$  and  $\beta$  as in panels (c,d), at the last computed time, namely (a)  $t = 31.613$  with  $k = 0.25$ , and (b)  $t = 116.960$  with  $k = 0.5$ . These snapshots evidence that cell-substrate friction is responsible for producing a secondary fingering instability in the nonlinear regime. In the absence of friction, the initial perturbation grows according to the linear analysis, i.e. non-trivially in time and remaining spatially harmonic during the whole time evolution, as shown in Figs. 1(d) and 2(b,c). This secondary instability resembles the tip-splitting phenomenon in the classical hydrodynamic Saffman-Taylor instability, which occurs for small values of the surface tension coefficient between the two fluids. It is also interesting to point out that, after the initially harmonic shape is destabilised into more finger-like structures, the fluid interface can eventually develop Eden-like structures<sup>67</sup> when  $\Lambda = 1$  in panel (e), and even more pronounced sulci when  $\Lambda = 8$  in panel (f), similar to the ones observed in many everyday-life phenomena and biological processes<sup>68-73</sup>.

### 4.4 The role of contractility

We now focus our attention to the effect of contractile stresses, that is  $\alpha < 0$ , on the monolayer spreading dynamics. To this end, we first compute the velocity field corresponding with the flat-front solution, which reads

$$\mathbf{u}_0 = \left[ \frac{\alpha \text{csch}(\Lambda L_0)}{2\Lambda} \left( \frac{\sinh(\Lambda y)}{\alpha \Lambda \left( \frac{\beta}{2\Lambda^2} - 1 \right)} - \frac{\text{csch}(\Lambda L_0) \sinh(2\Lambda y)}{\frac{\beta}{2\Lambda^2} - 4} \right) + \frac{\alpha \text{sech}(\sqrt{\beta/2}L_0)}{2\sqrt{\beta/2}} \left( 1 - \frac{\coth(\Lambda L_0)}{\alpha \Lambda \left( \frac{\beta}{2\Lambda^2} - 1 \right)} + \frac{2(1 + \coth(\Lambda L_0)^2)}{\frac{\beta}{2\Lambda^2} - 4} \right) \right] \sinh(\sqrt{\beta/2}y) \mathbf{e}_y. \quad (15)$$

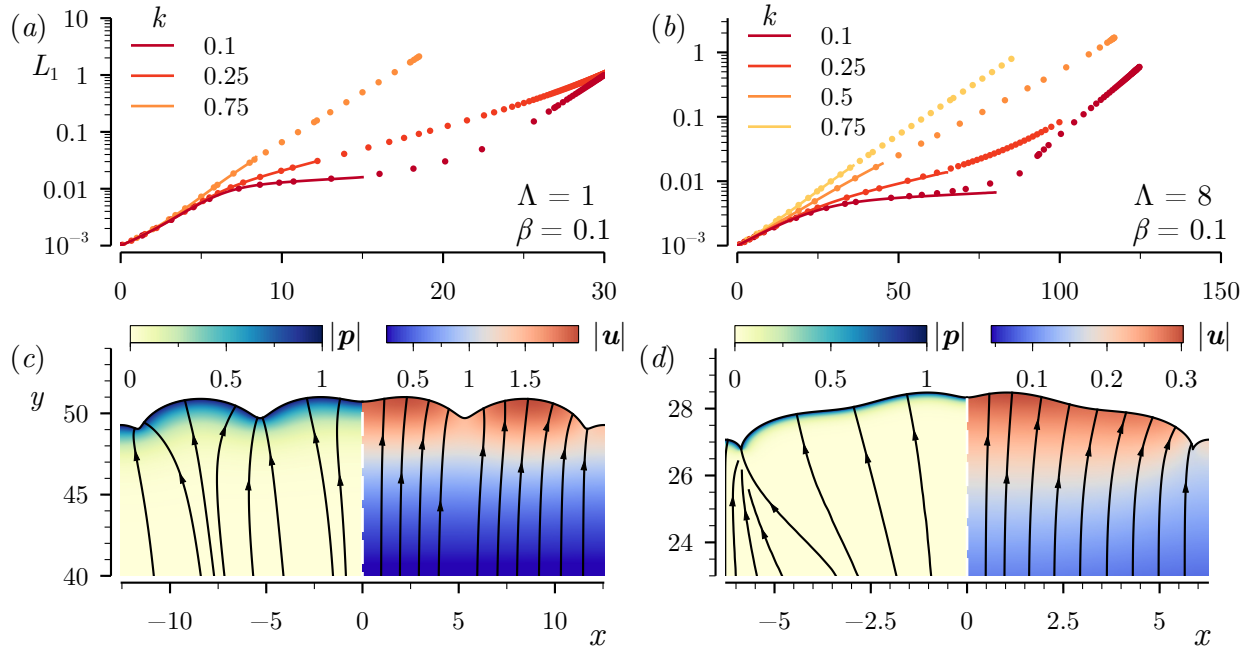


**Fig. 4** (a,b) Base flow interface  $L_0$  for (a)  $\Lambda = 1$  and (b)  $\Lambda = 8$  as a function of time  $t$  for different values of  $\beta$  indicated in the legends. (c,d) Perturbation amplitude  $L_1$  as a function of time  $t$  for different values of the wavenumber  $k$  indicated in the legends, for  $\beta = 0.1$ , (a)  $\Lambda = 1$ , and (b)  $\Lambda = 8$ . (e,f) Snapshot of the monolayer edge in the nonlinear regime showing  $|\mathbf{u}|$  and  $|\mathbf{p}|$ , for  $\beta = 0.1$ , (a)  $\Lambda = 1$ ,  $k = 0.25$ ,  $t = 31.613$ , (b)  $\Lambda = 8$ ,  $k = 0.5$ ,  $t = 116.960$ .

Due to contractility, the above expression exhibits a maximum value within the bulk, as opposed to the previous limiting cases. In particular, the stream-wise position of maximum velocity depends on the characteristic polarization length, that is  $y_{\max} \sim \Lambda^{-1}$ . For large values of  $\Lambda$ , the maximum velocity is located close to the edge since the monolayer is weakly polarised in the bulk, whereas for order-unity and small values of  $\Lambda$ , the maximum velocity is located between the edge and the middle line, approximately. This can be observed in Figs. 5(a,b), where  $u_y^0(y)$  is shown at different times for  $\Lambda = 1$ ,  $\beta = 1$ , and (a)  $\alpha = -0.9$ , (b)  $\alpha = -1$ . Additionally, these two panels show that, due to contractile stresses, the flat-front velocity at the edge  $\mathbf{u}_0(L_0)$  can be negative depending on the values of the dimensionless parameters. Indeed, we can define a critical contractile number,  $\alpha_c < 0$ , which characterises the usually referred to as active wetting-dewetting transition<sup>53,54</sup>, and whose analytical solution is given by the following expression:

$$\alpha_c = \frac{2(\beta - 8\Lambda^2) \left[ \sqrt{\beta} - \sqrt{2}\Lambda \coth(\Lambda) \tanh(\sqrt{\beta}/2) \right]}{(\beta - 2\Lambda^2) \left[ \sqrt{2}(\beta + 4\Lambda^2 \operatorname{csch}(\Lambda)^2) \tanh(\sqrt{\beta}/2) - 4\sqrt{\beta}\Lambda \coth(\Lambda) \right]}, \quad (16)$$

at which  $u_y^0(L_0) = 0$ , meaning that  $L_0$  remains quiescent at its initial value. Below this critical value,  $\alpha < \alpha_c$ , the monolayer contracts with time (dewetting), while for  $\alpha > \alpha_c$  the monolayer expands (wetting). Fig. 6 shows a colour plot of  $\alpha_c$  as a function of  $\beta$  and  $\Lambda$  in (a), and  $\alpha_c$  at constant values of  $\beta$  and  $\Lambda$  in (b,c), respectively. In particular, the absolute value of the critical contractility  $|\alpha_c|$  decreases monotonically as friction increases for every value of  $\Lambda$ , meaning that a smaller contractile stress is needed for the monolayer to retract as friction becomes dominant. Indeed,  $\alpha_c \rightarrow 0$  as  $\beta \rightarrow \infty$ . Moreover,  $|\alpha_c|$  increases monotonically with

$\Lambda$  for every finite value of  $\beta$ , which means that larger contractile stresses are needed for the monolayer to retract when it is weakly polarized within the bulk.

The critical transition obtained in the flat-front solution is reflected in Figs. 5(c) and (e-g), where we show  $L_0$  as a function of time  $t$  for the expanding ( $\alpha = -0.9$ ), contracting ( $\alpha = -1$ ), and steady-state ( $\alpha = \alpha_c \simeq -0.964$ ) cases, and three corresponding snapshots displaying  $|\mathbf{u}|$  at the last computed time, for  $\Lambda = \beta = 1$ , and  $k = 0.1$ . Additionally, Fig. 5(d) shows the perturbation amplitude  $L_1$  as a function of time  $t$  for the three different cases considered in panel (c), obtained from linear theory (solid lines), i.e eqn (11), and from numerical simulations (filled circles), displaying a perfect agreement in the linear regime. In the critical case,  $\alpha = \alpha_c$ , the monolayer edge grows exponentially in the linear regime since initially  $\mathbf{u}(L, t = 0) = \mathbf{0}$ . As time evolves, the monolayer adopts a rounded shape without developing a significant number of finger-like protrusions at the edge, as displayed in the snapshot in panel (f). When  $\alpha > \alpha_c$ , the monolayer expands and eventually develops a secondary fingering instability with a smaller characteristic wavelength, similarly to the case with negligible contractile stresses discussed in Sec. 3. Under dewetting conditions,  $\alpha < \alpha_c$ , the monolayer retracts, and although the perturbation amplitude initially grows, it decays at sufficiently long time, thus evidencing the importance of assessing the time-dependent stability of the moving front. Indeed, we have found that the flow generated by the retracting front is able to stabilise all wavenumbers. This can be explained alluding to the local friction at the edge, which increases as the retraction velocity becomes larger, as shown in Fig. 5(b). Examining the dependence of  $\omega(k, t)$  on  $\beta$ , we find that, when friction domi-

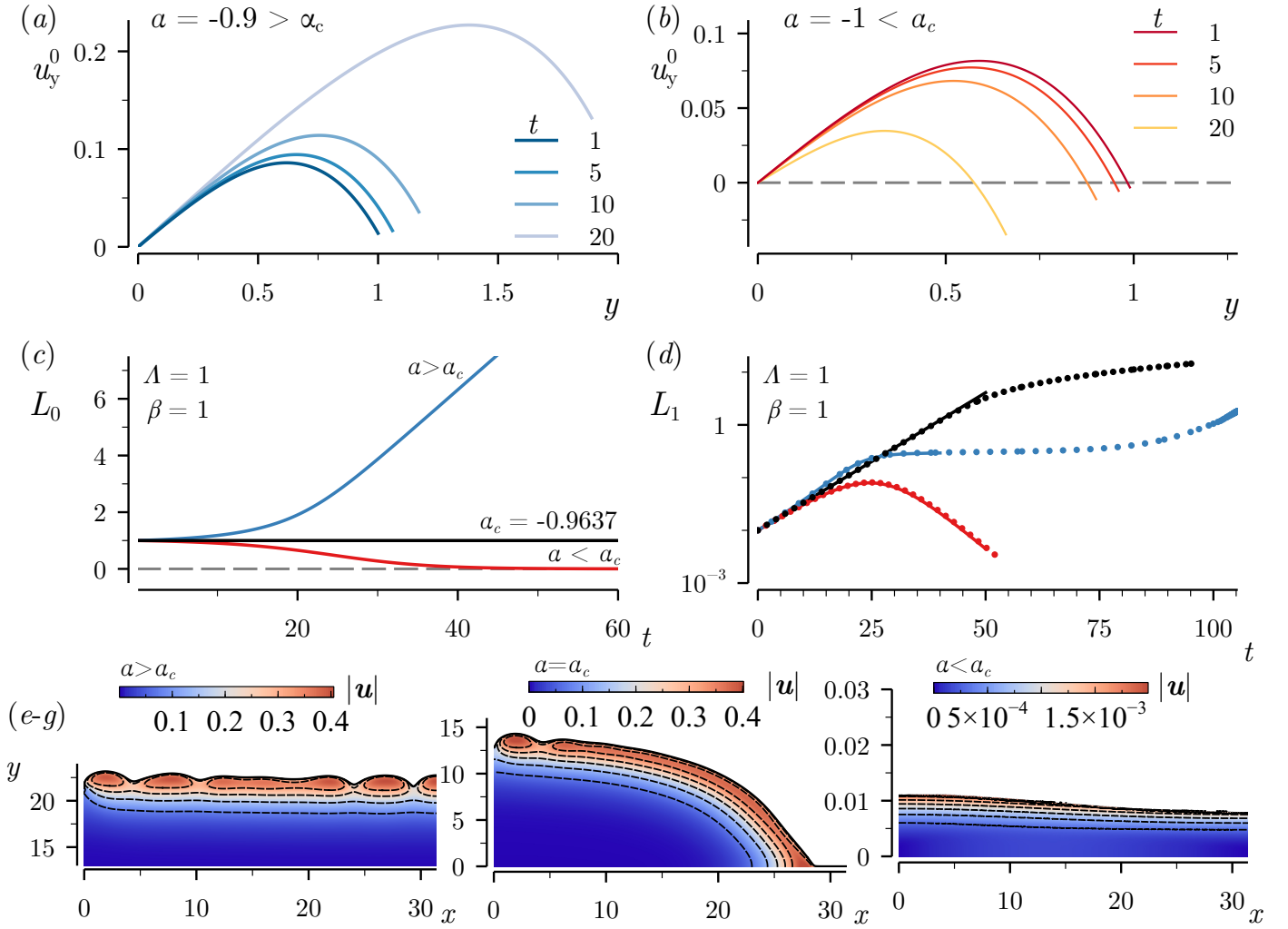


**Fig. 5** (a,b) Flat-front velocity field  $u_y^0(y)$  at different times indicated in the legend, for  $\Lambda = 1$ ,  $\beta = 1$ , (a)  $\alpha = -0.9 > \alpha_c$ , and (b)  $\alpha = -1 < \alpha_c$ . (c) Flat-front edge time evolution  $L_0(t)$  for the same values of  $\Lambda$  and  $\beta$ ,  $k = 0.1$ , and the three cases considered for  $\alpha$ , namely expanding  $\alpha = -0.9$ , contracting  $\alpha = -1$ , and marginally quiescent state  $\alpha \simeq -0.96$ . (d) Time evolution of the perturbation amplitude  $L_1(t)$  for the same values as in (c). Panels (e-g) show snapshots of the three cases considered in (c,d)

nates, i.e. for a large value of  $\beta$ , the maximum growth rate  $\omega_m$  becomes negative, thus the whole amplification curve becomes negative. This is depicted in Fig. 8, which shows the short-time maximum growth rate  $\omega_{S,m}$  and the corresponding most amplified wavenumber  $k_{S,m}$  as functions of  $\Lambda$  and  $\beta$  for (a,b)  $\alpha = 0$  and (c,d)  $\alpha = -1$ .

Finally, Fig. 7 displays different snapshots at long time in the parameter space  $(\Lambda, \beta)$  for  $\alpha \gtrsim \alpha_c$  and  $k = 0.1$ . For negligible friction,  $\beta = 0$ , these morphologies evidence that the shape of the front remains harmonic for long times, even when contractile stresses play a role. Thus, the main mechanism responsible for tip-splitting phenomena and secondary fingering instabilities is solely cell-substrate friction. Furthermore, for increasing values of  $\Lambda$  and  $\beta$ , the characteristic wavelength of the secondary instability decreases and the finger-like structures at the edge become more complex. Fig. 8 shows that the most amplified wavenumber increases, and therefore the wavelength decreases, when  $\beta$  and  $\Lambda$  increase. This occurs locally at the edge of the tissue, as the front

migrates and the velocity increases.

## 5 Concluding remarks and future prospects

Motivated by observations of interfacial instabilities in biological contexts during in vivo and in vitro processes, here we have analysed some of the main mechanisms involved in the appearance of finger-like instabilities in migrating epithelial monolayers. To this end, we have modelled the monolayer as a continuum compressible polar fluid and analysed the linear and nonlinear dynamics of the spreading front. By means of linear stability analyses and numerical simulations, we have unravelled the roles of cell polarization, substrate friction, and contractile stresses.

Regarding the linear stability of the spreading front, we have shown that it is crucial to analyse the transient dynamics of the perturbation amplitude  $L_1$ , since, although it initially grows exponentially in time, it eventually develops non-trivial transient dynamics. In particular, in the limit when cell-substrate friction and contractile stresses are negligible, there is finite most unsta-

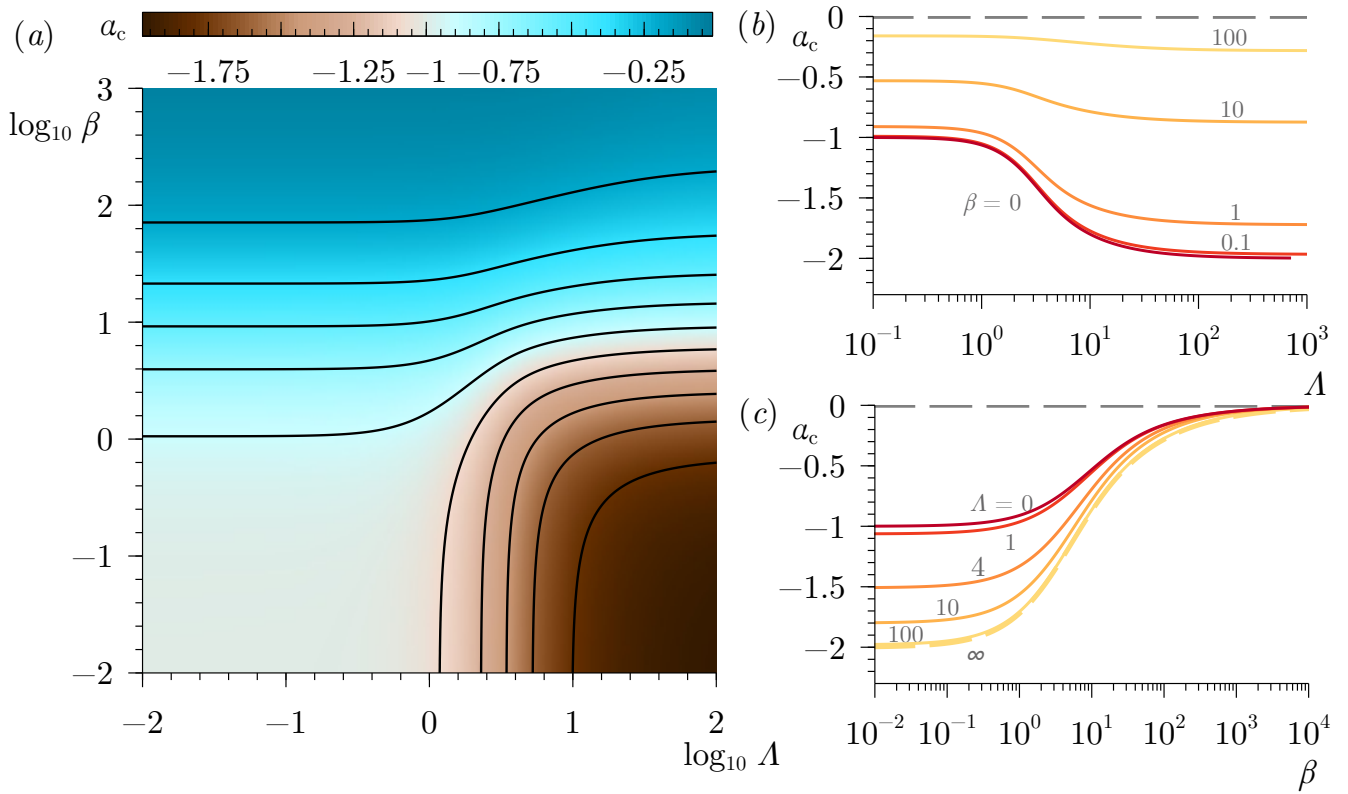


**Fig. 6** (a) Contour plot of the critical contractile number  $\alpha_c$  as a function of  $\Lambda$  and  $\beta$ . Panels (b,c) show  $\alpha_c$  as a function of  $\Lambda$  and  $\beta$  for different constant values of  $\beta$  and  $\Lambda$ , respectively.

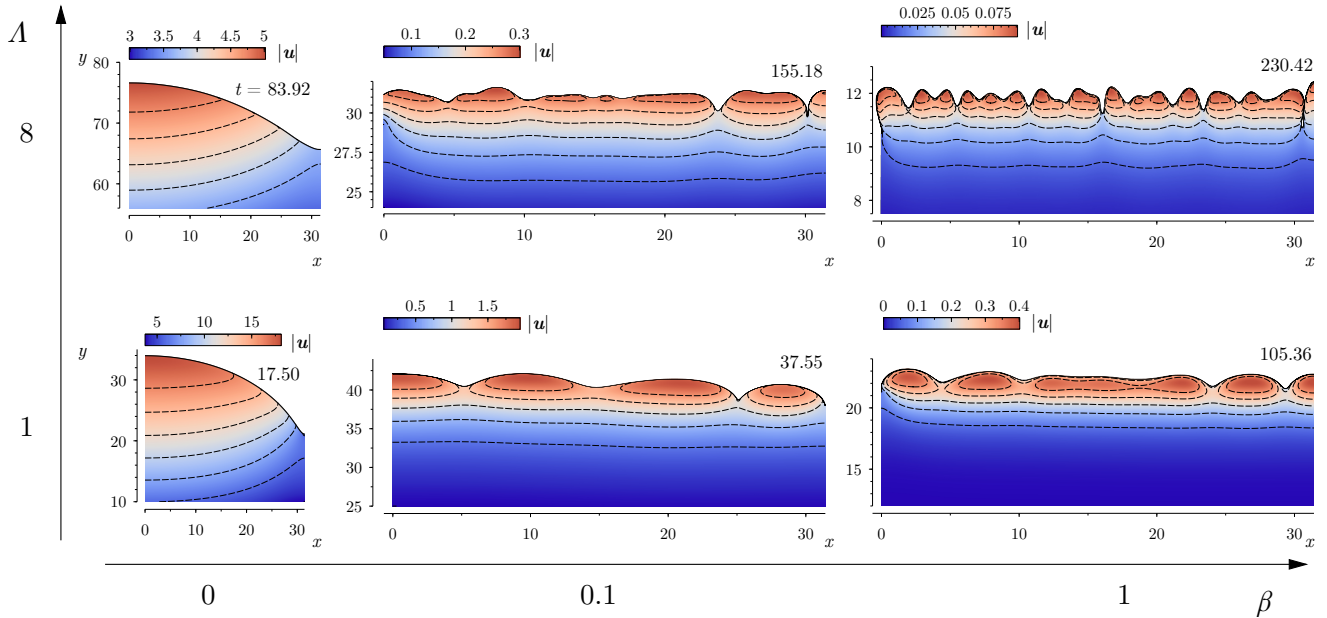


**Fig. 7** Snapshots of the spreading monolayer in the parameter space  $(\Lambda, \beta)$ , for  $k = 0.1$ ,  $\alpha = -1$  in the top row ( $\Lambda = 8$ ), and  $\alpha = -0.9$  in the bottom row ( $\Lambda = 1$ ). Times are indicated in the labels.

ble wavenumber at short times<sup>42</sup>, but at long time,  $L_1$  eventually grows faster for monotonically decreasing values of  $k$ . This is possible since, for small values of  $k$ ,  $L_1$  experiences several crossovers between different exponential regimes. Additionally, in this limiting case, the linear stability analysis is able to describe the tran-

sient evolution of the spreading monolayer even at large times when  $L_1 \sim O(1)$ , meaning that the growth of  $L_1$  remains linear and spatially harmonic.

Only when cell-substrate friction is considered, secondary finger-like structures arise in the nonlinear regime, similar to the

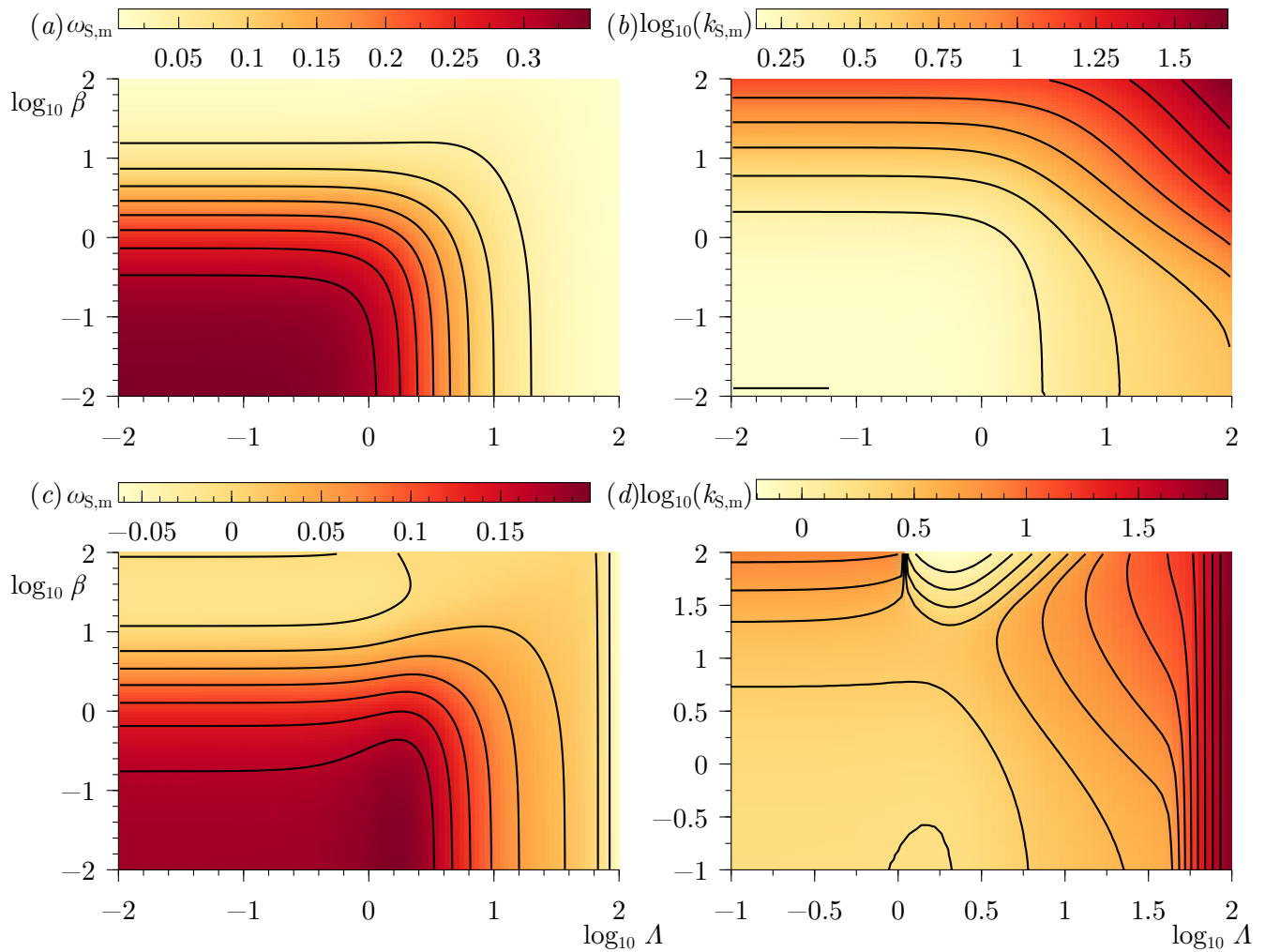


**Fig. 8** Short-time maximum growth rate  $\omega_{S,m}$  and the corresponding most amplified wavenumber  $k_{S,m}$ , as functions of  $\Lambda$  and  $\beta$ , for (a,b)  $\alpha = 0$ , and (c,d)  $\alpha = -1$ .

ones observed in many biological processes. In this scenario, the linear stability analysis is of limited value, as it is quantitatively valid only when the perturbation amplitude remains small,  $L_1 \lesssim 10^{-2}$ . Above this value, secondary edge instabilities arise. Additionally, the fingering pattern becomes more complex when cell-substrate friction becomes dominant and the edge of the monolayer is strongly polarized. This result of linear stability analysis could potentially explain the onset of fingering instabilities. It suggests that fingering instabilities appearing in in vivo and in vitro experiments may be a direct consequence of cell-substrate friction.

Finally, when contractile stresses are taken into account, we have obtained a critical contractility,  $\alpha_c < 0$ , at which the monolayer displays a quiescent polarized steady state, thus characterising the active wetting-dewetting transition<sup>54</sup>. Below this critical value, the monolayer expands (wetting), and above it contracts (dewetting). Additionally, in the latter scenario, we have observed that, although the monolayer is initially unstable, it eventually becomes stable as the edge retracts, thus evidencing the importance of assessing the time-dependent evolution of the

perturbation amplitude.

Although our work shows that cell-substrate friction is crucial to trigger the formation of finger-like structures at the edge of a migrating epithelial monolayer, a thorough comparison with controlled experiments would be necessary to clarify these theoretical and numerical results. From a theoretical point of view, cell proliferation would likely play a relevant role during cell migration and the formation of finger-like protrusions, thus the effect of incorporating a density field and a density-dependent pressure deserves further investigation. Other natural extensions of our work include the effect of noise, rheology, durotaxis, coupling between flow and cell polarization, or chemical signaling, both, on the linear and nonlinear dynamics.

## Conflicts of interest

There are no conflicts to declare.

## Acknowledgements

CT and LLB acknowledge financial support by the FEDER/Ministerio de Ciencia, Innovación y Universidades – Agencia Estatal de Investigación grant MTM2017-84446-C2-2-R,

by the Madrid Government (Comunidad de Madrid-Spain) under the Multiannual Agreement with UC3M in the line of Excellence of University Professors (EPUC3M23), and in the context of the V PRICIT (Regional Programme of Research and Technological Innovation). AM-C also acknowledges financial support by the FEDER/Ministerio de Ciencia, Innovación y Universidades – Agencia Estatal de Investigación through the project DPI2017-88201-C3-3-R, and the Red Nacional para el Desarrollo de la Microfluidica, RED2018-102829-T. The authors warmly acknowledge Ricard Alert-Zenón for useful comments and insightful advice.

## Notes and references

- 1 S. Hill, *Chem. Eng. Sci.*, 1952, **1**, 247–253.
- 2 R. Chuoke, P. Van Meurs and C. van der Poel, *Trans. AIME*, 1959, **216**, 188–194.
- 3 P. Saffman and G. I. Taylor, *Proc. R. Soc. Lond. A*, 1958, **245**, 312–329.
- 4 H. S. Hele-Shaw, *Trans. Instn. Nav. Archit., Lond.*, 1898, **40**, 21.
- 5 D. Bensimon, L. P. Kadanoff, S. Liang, B. I. Shraiman and C. Tang, *Rev. Mod. Phys.*, 1986, **58**, 977.
- 6 G. M. Homsy, *Annu. Rev. Fluid Mech.*, 1987, **19**, 271–311.
- 7 D. A. Kessler, J. Koplik and H. Levine, *Adv. Phys.*, 1988, **37**, 255–339.
- 8 A. Oron, S. H. Davis and S. G. Bankoff, *Rev. Mod. Phys.*, 1997, **69**, 931.
- 9 E. Ben-Jacob, I. Cohen and H. Levine, *Adv. Phys.*, 2000, **49**, 395–554.
- 10 E. Ben-Jacob, H. Shmueli, O. Shochet and A. Tenenbaum, *Physica A*, 1992, **187**, 378–424.
- 11 E. Ben-Jacob, O. Schochet, A. Tenenbaum, I. Cohen, A. Czirok and T. Vicsek, *Nature*, 1994, **368**, 46–49.
- 12 J. A. Shapiro, *BioEssays*, 1995, **17**, 597–607.
- 13 D. B. Kearns, *Nat. Rev. Microbiol.*, 2010, **8**, 634–644.
- 14 E. Ben-Jacob, D. S. Coffey and H. Levine, *Trends Microbiol.*, 2012, **20**, 403–410.
- 15 F. Farrell, O. Hallatschek, D. Marenduzzo and B. Waclaw, *Phys. Rev. Lett.*, 2013, **111**, 168101.
- 16 T. Lecuit, P.-F. Lenne and E. Munro, *Annu. Rev. Cell Dev. Biol.*, 2011, **27**, 157–184.
- 17 K. Goodwin, S. Mao, T. Guyomar, E. Miller, D. C. Radisky, A. Košmrlj and C. M. Nelson, *Development*, 2019, **146**.
- 18 B. A. Nerger, J. M. Jaslove, H. E. Elashal, S. Mao, A. Košmrlj, A. J. Link and C. M. Nelson, *Curr. Biol.*, 2021.
- 19 G. Forgacs and S. A. Newman, *Biological Physics of the Developing Embryo*, Cambridge University Press, 2005.
- 20 T. Lecuit and P.-F. Lenne, *Nat. Rev. Mol. Cell Biol.*, 2007, **8**, 633–644.
- 21 M. Abercrombie and E. Ambrose, *Cancer Res.*, 1962, **22**, 525–548.
- 22 P. Friedl and D. Gilmour, *Nat. Rev. Mol. Cell Biol.*, 2009, **10**, 445–457.
- 23 K. J. Streitberger, L. Lilaj, F. Schrank, J. Braun, K. T. Hoffmann, M. Reiss-Zimmermann, J. A. Käs and I. Sack, *Proc. Natl. Acad. Sci. U.S.A.*, 2020, **117**, 128–134.
- 24 S. Moitrier, C. Blanch-Mercader, S. Garcia, K. Sliogeryte, T. Martin, J. Camonis, P. Marcq, P. Silberzan and I. Bonnet, *Soft Matter*, 2019, **15**, 537–545.
- 25 L. L. Bonilla, A. Carpio and C. Trenado, *PLoS Comput. Biol.*, 2020, **16**, e1008407.
- 26 R. Mayor and S. Etienne-Manneville, *Nat. Rev. Mol. Cell Biol.*, 2016, **17**, 97.
- 27 B. Stramer and R. Mayor, *Nat. Rev. Mol. Cell Biol.*, 2017, **18**, 43–55.
- 28 B. Ladoux and R.-M. Mège, *Nat. Rev. Mol. Cell Biol.*, 2017, **18**, 743–757.
- 29 W. Xi, T. B. Saw, D. Delacour, C. T. Lim and B. Ladoux, *Nat. Rev. Mat.*, 2019, **4**, 23–44.
- 30 R. Alert and X. Trepat, *Annu. Rev. Cond. Matter Phys.*, 2020, **11**, 77–101.
- 31 R. Hooke, *Micrographia: or some physiological descriptions of minute bodies made by magnifying glasses, with observations and inquiries thereupon*, Courier Corporation, 2003.
- 32 T. Omelchenko, J. M. Vasiliev, I. M. Gelfand, H. H. Feder and E. M. Bonder, *Proc. Natl. Acad. Sci. U.S.A.*, 2003, **100**, 10788–10793.
- 33 M. Poujade, E. Grasland-Mongrain, A. Hertzog, J. Jouanneau, P. Chavrier, B. Ladoux, A. Buguin and P. Silberzan, *Proc. Natl. Acad. Sci. U.S.A.*, 2007, **104**, 15988–15993.
- 34 S. Begnaud, T. Chen, D. Delacour, R.-M. Mège and B. Ladoux, *Curr. Opin. Cell Biol.*, 2016, **42**, 52–62.
- 35 M. Vishwakarma, J. Di Russo, D. Probst, U. S. Schwarz, T. Das and J. P. Spatz, *Nat. Comm.*, 2018, **9**, 1–12.
- 36 Y. Yang and H. Levine, *Phys. Biol.*, 2020, **17**, 046003.
- 37 J. J. Williamson and G. Salbreux, *Phys. Rev. Lett.*, 2018, **121**, 238102.
- 38 N. Sepúlveda, L. Petitjean, O. Cochet, E. Grasland-Mongrain, P. Silberzan and V. Hakim, *PLoS Comput. Biol.*, 2013, **9**, e1002944.
- 39 V. Tarle, A. Ravasio, V. Hakim and N. S. Gov, *Integr. Biol.*, 2015, **7**, 1218–1227.
- 40 M. Basan, J. Elgeti, E. Hannezo, W. J. Rappel and H. Levine, *Proc. Natl. Acad. Sci. U.S.A.*, 2013, **110**, 2452–2459.
- 41 D. Nesbitt, G. Pruessner and C. F. Lee, *Phys. Rev. E*, 2017, **96**, 062615.
- 42 R. Alert, C. Blanch-Mercader and J. Casademunt, *Phys. Rev. Lett.*, 2019, **122**, 088104.
- 43 J. Zimmermann, M. Basan and H. Levine, *Eur. Phys. J. Spec. Top.*, 2014, **223**, 1259–1264.
- 44 M. J. Bogdan and T. Savin, *R. Soc. Open Sci.*, 2018, **5**, 181579.
- 45 S. Mark, R. Shlomovitz, N. S. Gov, M. Poujade, E. Grasland-Mongrain and P. Silberzan, *Biophys. J.*, 2010, **98**, 361–370.
- 46 P. B. Canham, *J. Theor. Bio.*, 1970, **26**, 61–81.
- 47 W. Helfrich, *Z. Naturforsch. C.*, 1973, **28**, 693–703.
- 48 O. Y. Zhong-Can and W. Helfrich, *Phys. Rev. Lett.*, 1987, **59**, 2486.

- 49 O.-Y. Zhong-Can and W. Helfrich, *Phys. Rev. A*, 1989, **39**, 5280.
- 50 U. Seifert and S. A. Langer, *EPL*, 1993, **23**, 71.
- 51 U. Seifert, *Adv. Phys.*, 1997, **46**, 13–137.
- 52 C. Blanch-Mercader, R. Vincent, E. Bazellieres, X. Serra-Picamal, X. Trepap and J. Casademunt, *Soft Matter*, 2017, **13**, 1235–1243.
- 53 R. Alert and J. Casademunt, *Langmuir*, 2018, **35**, 7571–7577.
- 54 C. Pérez-González, R. Alert, C. Blanch-Mercader, M. Gómez-González, T. Kolodziej, E. Bazellieres, J. Casademunt and X. Trepap, *Nat. Phys.*, 2019, **15**, 79–88.
- 55 M. A. Heinrich, R. Alert, J. M. LaChance, T. J. Zajdel, A. Košmrlj and D. J. Cohen, *Elife*, 2020, **9**, e58945.
- 56 P. Lee and C. W. Wolgemuth, *PLoS Comput. Biol.*, 2011, **7**, e1002007.
- 57 M. H. Köpf and L. M. Pismen, *Soft Matter*, 2013, **9**, 3727–3734.
- 58 X. Trepap, M. R. Wasserman, T. E. Angelini, E. Millet, D. A. Weitz, J. P. Butler and J. J. Fredberg, *Nat. Phys.*, 2009, **5**, 426–430.
- 59 R. A. Foty, G. Forgacs, C. M. Pfleger and M. S. Steinberg, *Phys. Rev. Lett.*, 1994, **72**, 2298.
- 60 J. Prost, F. Jülicher and J. F. Joanny, *Nat. Phys.*, 2015, **11**, 111–117.
- 61 P. G. De Gennes and J. Prost, *The physics of liquid crystals*, Oxford university press, 1993, vol. 83.
- 62 P.-G. de Gennes, *C. R. Acad. Sci.*, 1979, **228B**, 219.
- 63 F. Brochard and P. G. De Gennes, *Langmuir*, 1992, **8**, 3033–3037.
- 64 F. Brochard-Wyart, G. Debregeas, R. Fondécave and P. Martin, *Macromolecules*, 1997, **30**, 1211–1213.
- 65 A. Martínez-Calvo, J. Rivero-Rodríguez, B. Scheid and A. Sevilla, *J. Fluid Mech.*, 2020, **883**, A35.
- 66 D. Moreno-Boza, A. Martínez-Calvo and A. Sevilla, *Phys. Rev. Fluids*, 2020, **5**, 014002.
- 67 M. Eden, Fourth Berkeley Symp. Math Stat. Prob., 1961, pp. 223–239.
- 68 E. Hohlfeld and L. Mahadevan, *Phys. Rev. Lett.*, 2011, **106**, 105702.
- 69 E. Hohlfeld and L. Mahadevan, *Phys. Rev. Lett.*, 2012, **109**, 025701.
- 70 A. E. Shyer, T. Tallinen, N. L. Nerurkar, Z. Wei, E. S. Gil, D. L. Kaplan, C. J. Tabin and L. Mahadevan, *Science*, 2013, **342**, 212–218.
- 71 T. Tallinen, J. S. Biggins and L. Mahadevan, *Phys. Rev. Lett.*, 2013, **110**, 024302.
- 72 T. Tallinen, J. Y. Chung, J. S. Biggins and L. Mahadevan, *Proc. Natl. Acad. Sci. U.S.A.*, 2014, **111**, 12667–12672.
- 73 T. Tallinen, J. Y. Chung, F. Rousseau, N. Girard, J. Lefèvre and L. Mahadevan, *Nat. Phys.*, 2016, **12**, 588–593.